AGU ADVANCING EARTH AND SPACE SCIENCES

Space Weather®

Key Points:
- Observed properties of solar magnetic storms concurrent with the loss of Starlink satellites are analyzed in this study
- Physical and empirical models are used to study near-Earth space weather conditions, enhanced drag and orbital decay of the Starlink satellites
- Our study shows that space weather conditions, low-altitude insertion and some physical satellite attributes together led to this mishap

Supporting Information:
Supporting Information may be found in the online version of this article.

Correspondence to:
D. Nandy,
dnandi@iiserkol.ac.in

The Loss of Starlink Satellites in February 2022: How Moderate Geomagnetic Storms Can Adversely Affect Assets in Low-Earth Orbit

Yoshita Baruah[1,2] ⓘ, **Souvik Roy[2]** ⓘ, **Suvadip Sinha[2]** ⓘ, **Erika Palmerio[3]** ⓘ, **Sanchita Pal[4]** ⓘ, **Denny M. Oliveira[4,5]** ⓘ, and **Dibyendu Nandy[1,2]** ⓘ

[1]Department of Physical Sciences, Indian Institute of Science Education and Research Kolkata, Mohanpur, India, [2]Center of Excellence in Space Sciences India, Indian Institute of Science Education and Research Kolkata, Mohanpur, India, [3]Predictive Science Inc., San Diego, CA, USA, [4]Heliophysics Science Division, NASA Goddard Space Flight Center, Greenbelt, MD, USA, [5]Goddard Planetary Heliophysics Institute, University of Maryland, Baltimore, MD, USA

Abstract On 3 February 2022, SpaceX launched 49 Starlink satellites, 38 of which unexpectedly de-orbited. Although this event was attributed to space weather, definitive causality remained elusive because space weather conditions were not extreme. In this study, we identify solar sources of the interplanetary coronal mass ejections that were responsible for the geomagnetic storms around the time of launch of the Starlink satellites and for the first time, investigate their impact on Earth's magnetosphere using magnetohydrodynamic modeling. The model results demonstrate that the satellites were launched into an already disturbed space environment that persisted over several days. However, on performing comparative satellite orbital decay analyses, we find that space weather alone was not responsible but conspired together with a low-altitude insertion and low satellite mass-to-area ratio to precipitate this unusual loss. Our work bridges space weather causality across the Sun–Earth system—with relevance for space-based human technologies.

Plain Language Summary Human society is becoming increasingly dependent on satellites at Low Earth Orbit (LEO) which cater to Earth observations, telecommunications, navigation and defense needs. The impact of space weather–changing environmental conditions in space governed by the Sun–at Low Earth Orbits is only beginning to be appreciated. The loss of an unprecedented number of Starlink satellites after their launch on 3 February 2022, which was attributed to space weather, is a case in point. Surprisingly, solar magnetic storms and space weather conditions around the time of the launch of the Starlink satellites were quite modest, making it challenging to establish physical causality. Here we utilize a multipronged approach based on observations of solar magnetic storms, near-Earth environmental conditions and novel computer simulations to establish causality between the prevailing space environmental conditions at LEO and the loss of the satellites. Our comprehensive analysis reveals that the loss of the satellites was due to a combination of factors including prevalent space weather conditions, an insertion at a relatively high-density LEO and possibly enhanced drag due to orientation changes of the satellites accentuated by a relatively high drag to inertia ratio.

1. Introduction

SpaceX launched 49 Starlink satellites on 3 February 2022 into an orbit with a perigee of approximately 210 km. On 4 February 2022, many of these satellites started de-orbiting. Eventually, within a couple of days, 38 of them were lost, entailing a significant economic loss of millions of dollars (Hapgood et al., 2022).

This incident is a classic example of how human society is becoming more vulnerable to the effects of space weather with our increasing dependence on technology (Schrijver et al., 2015). Space weather encompasses the influence that the dynamic conditions of the Sun have on the near-Earth space environment (Nandy et al., 2023). It is orchestrated by various explosive events on the Sun such as solar flares, coronal mass ejections (CMEs), solar energetic particle events, and radio bursts (Riley et al., 2018). Among the most significant terrestrial manifestations of such events are geomagnetic storms (Gosling et al., 1991). A primary agent of such storms are Earth-directed CMEs having a strong southward-pointing magnetic field (J. Zhang et al., 2007). High-speed streams (HSSs) of solar wind emanating from coronal holes can also drive weak-to-moderate geomagnetic storms (Tsurutani et al., 2006).

Table 1
List of Observed CMEs That Contributed to the Geomagnetic Perturbations on 3 and 4 February 2022.

Event no.	Time of CME appearance in LASCO C2 (UT)	CME apex location obtained from GCS (Lat, Lon)[a] (°, °)	3D CME speed from GCS (km s⁻¹)	Estimated Earth arrival time from DBEM[b] (UT)	Expected Earth arrival speed (km s⁻¹)	Probability of reaching Earth estimated by DBEM
1	2022-01-29 23:36	−6, 329	791	2022-02-01 15:15	573	99% hit
2	2022-01-31 16:10	15, 23	357	2022-02-05 02:44	413	99% hit
3	2022-02-01 07:12	17, 19	458	2022-02-05 04:23	439	98% hit

[a]Lat and Lon stand for the latitude and longitude in heliographic Coordinates. [b]DBEM stands for Drag-Based Ensemble Model (Čalogović et al., 2021).

The solar wind continuously deposits energy and particles into Earth's magnetosphere, but this is amplified during such storms. Approximately 60% of this energy is transferred into the atmosphere in the form of particle precipitation and dominantly, as Joule heating. This causes the thermosphere to heat up and expand upwards (Knipp et al., 2004; Oliveira et al., 2017). This results in an increase in the neutral mass density observed at the altitude of Low Earth Orbit (LEO) satellites, increasing the aerodynamic drag on them and contributing to enhancement in their orbital decay (Oliveira & Zesta, 2019).

Multiple studies have analyzed the solar eruptive events (e.g., Dang et al., 2022; Fang et al., 2022; Gopalswamy et al., 2023; Kataoka et al., 2022; Pal et al., 2023), Joule-heating-mediated changes in thermospheric conditions as a result of their interaction with Earth's magnetosphere (e.g., He et al., 2023; Laskar et al., 2023; Lin et al., 2022; Lockwood et al., 2023), thermospheric drag and orbital decay of the Starlink satellites (e.g., Berger et al., 2023; Guarnieri et al., 2023; Y. Zhang et al., 2022), as well as magnetospheric and ionospheric effects (e.g., Duann et al., 2023; Gulyaeva et al., 2023; Tsurutani et al., 2022; Tsyganenko et al., 2022) due to the geomagnetic storms of 3–4 February 2022. This is the first study that employs data-driven magnetohydrodynamic (MHD) modeling of Earth's magnetosphere, alongside detailed investigations of the near-Sun and near-Earth environments concurrent with the loss of the Starlink satellites, to interpret the physical processes that led to this mishap. In addition, we conduct empirical modeling of the satellite orbits, which illuminates the accentuation of atmospheric drag on the satellites due to certain satellite properties and low-altitude orbital insertion, elucidating how multiple factors together caused the Starlink satellites to re-enter the atmosphere. With more and more satellites being deployed at LEO for supporting humanity's space-based societal infrastructure, our findings are expected to inform the design and operational strategies of these space assets.

2. Solar Sources of the Moderate Geomagnetic Storms That Impacted the Starlink Satellites

We use coronagraph data from the Large Angle Spectroscopic Coronagraph (LASCO; Brueckner et al., 1995) on board the Solar and Heliospheric Observatory (SOHO; Domingo et al., 1995), and the COR2 telescope on the Sun-Earth Connection Coronal and Heliospheric Investigation (SECCHI; Howard et al., 2008) on board the Solar Terrestrial Relations Observatory Ahead (STEREO-A; Kaiser et al., 2008) for identification of possible Earth-directed CMEs that might have erupted from the Sun 1–5 days before the onset of the geomagnetic perturbations that impacted the Starlink satellites. During the period under investigation, STEREO-A was located ∼35° east of the Sun–Earth line. Consequently, we search for corresponding activity on the solar disc using extreme ultra-violet imagery from the Atmospheric Imaging Assembly (AIA; Lemen et al., 2012) instrument on board the Solar Dynamics Observatory (SDO; Pesnell et al., 2012) to locate the associated source regions.

Three CMEs have been distinctly identified whose estimated Earth arrival times fall between 1 and 5 February 2022. The kinematic and morphological details of the CMEs, determined using the Graduated Cylindrical Shell (GCS) model (Thernisien et al., 2006), are reported in Table 1. All three CMEs were associated with NOAA active region 12936, which was located at ∼17° North (in the Heliographic coordinate system) of the visible solar disk during the period under scrutiny. The first CME (henceforth CME1)—which accompanied an M1.0-class solar flare and erupted on 29 January 2022 at around 23:30 UT—was a halo event with a complex structure and was deflected southward toward the heliospheric current sheet. This can be observed in the separation between the
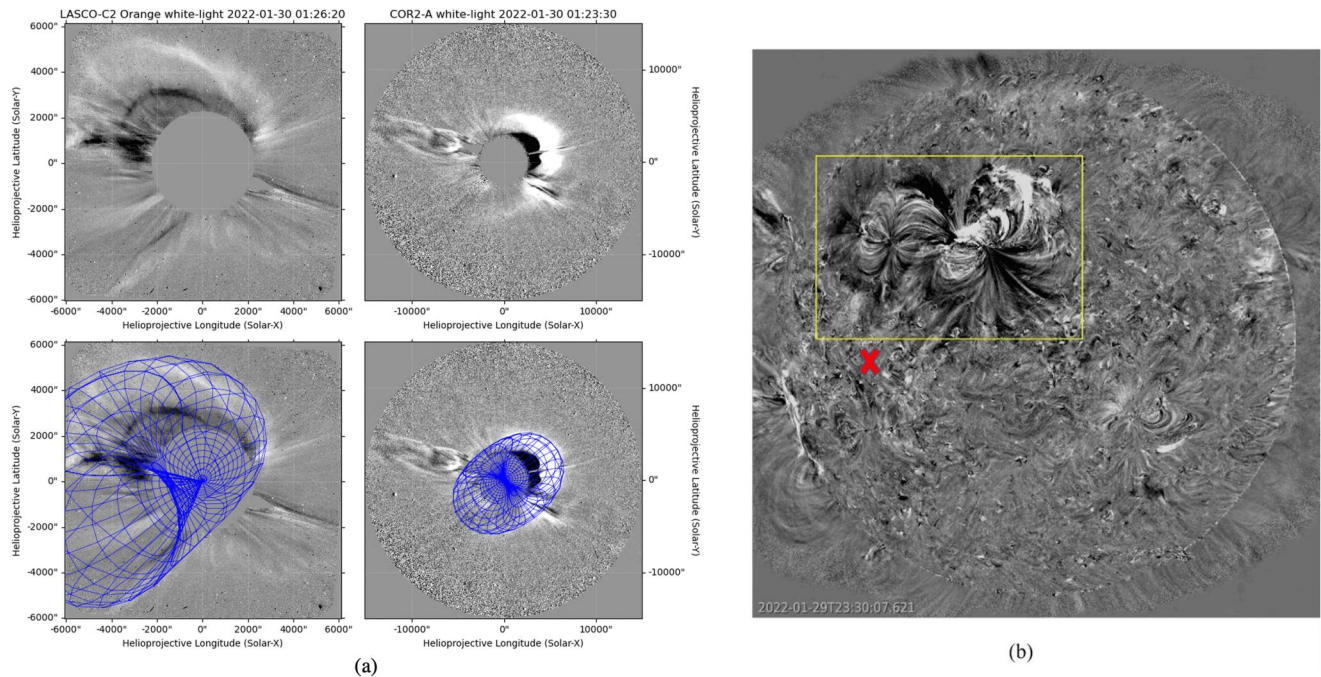
Figure 1. Remote-sensing observations of CME1. (a) The top row shows CME1 in the LASCO/C2 and STEREO/COR2-A fields of view, while the bottom row displays the Graduated Cylindrical Shell (GCS) wireframe fitted on CME1. (b) AIA 193 Å running-difference image of the CME1 eruption. The yellow box marks the coronal mass ejection (CME) source region, while the red cross indicates the projected propagation direction of the CME apex inferred via the GCS technique.

solar source signature of CME1 and the CME apex projected by the GCS model based on coronagraphs in the AIA 194 Å difference image of Figure 1. It was expected to arrive at Earth on 1 February 2022.

CME2 erupted on 31 January 2022 around 16:00 UT with weak low-coronal signatures (shown in Figure 2). Hence, we use image differencing over long time scales (10 hr) as they have proven to be useful in revealing such elusive eruptions (Nitta et al., 2021; Palmerio, Nitta, et al., 2021). The CME propagation direction estimated via the GCS technique is consistent with the location of a weak coronal dimming (often a signature of an erupting CME; e.g., Jin et al., 2022; Thompson et al., 2000), suggesting that CME2 did not experience significant deflections in the solar corona. It was slow and faint, with a near-sun speed of about 357 km/s. CME3 erupted on 1 February 2022 around 07:00 UT. Coronagraph imagery, GCS reconstructions, and source region for CME3 have been shown in Figure 3. A coronal dimming is identified as the source signature for this event. This event had a higher speed (458 km/s) than CME2, hence, it is likely that the two CMEs interacted during their interplanetary propagation. A recent study by Pal et al. (2023) analyzed the dynamics and interactions of CME1, CME2, and CME3 in the interplanetary medium in detail. They approximated the heliocentric distance where CME2 and CME3 possibly merged to be around ∼0.4 au. We calculate the Earth arrival times of the three CMEs using the Drag-Based Ensemble Model (DBEM; Čalogović et al., 2021), a simple yet powerful tool for associating near-Sun CME observations with corresponding interplanetary coronal mass ejection (ICME) signatures. We use an ambient solar wind speed of 450 km/s to estimate the Earth arrival time of all three CMEs, apriori making no assumption on the merger of CME2 and CME3. The typical error in arrival time estimation with DBEM for isolated CMEs is around 12 hr. We remark that DBEM is not efficient in providing arrival time information for a merged CME when the merging occurs in the path of CMEs' propagation toward Earth, but it is still useful for understanding the sequence of solar activities during the concerned period. Nonetheless, the predicted arrival times of CME2 and CME3 are ∼1.5 hr apart which is a much smaller time interval than the error range of ±12 hr; this is not inconsistent with the inference of merger based on in-situ observations. We also note that the challenges of predicting CME arrival times are manifested in CME 1 arriving 6 hr later than predicted, and CME2 and CME3 arriving a day earlier than predicted (discussed in Section 3). The earlier arrival of CME 2 and CME3 is possibly related to interactions with a HSS, which the DBEM model cannot account for.
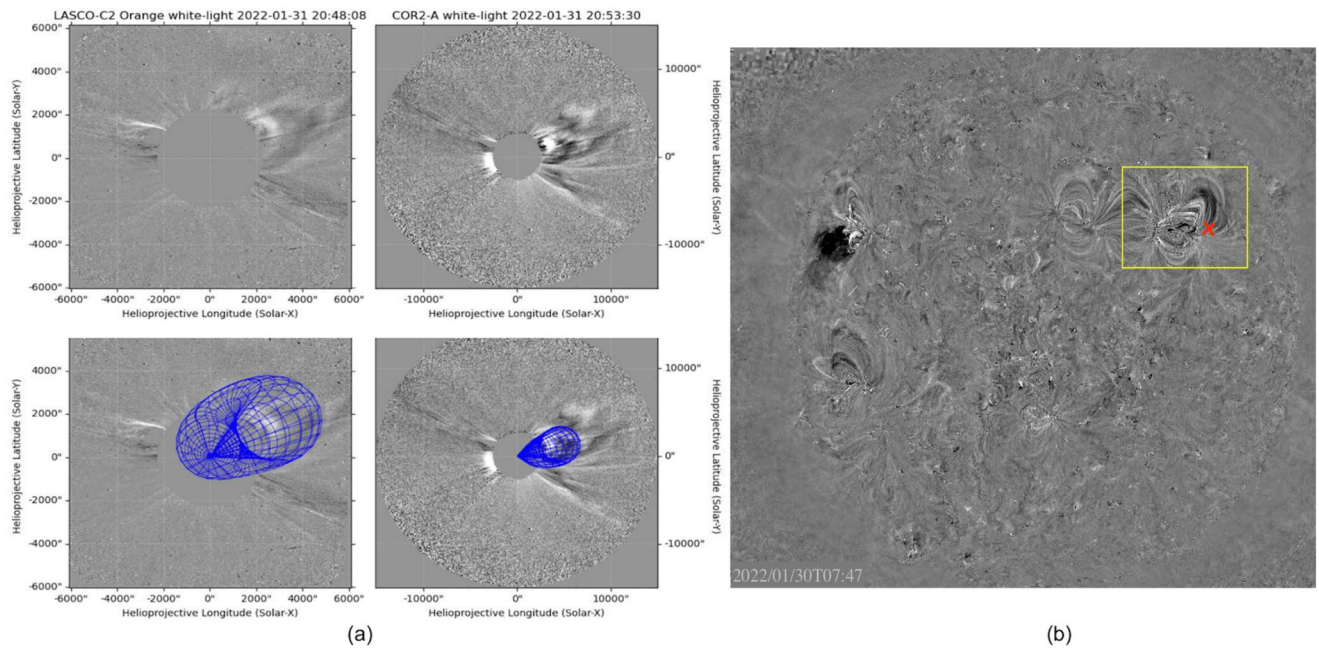
Figure 2. Remote-sensing observations of CME2. (a) The top row shows CME2 in the LASCO/C2 and STEREO/COR2-A fields of view, while the bottom row displays the Graduated Cylindrical Shell (GCS) flux rope wireframe fitted on CME2. (b) STEREO/EUVI-A 195 Å difference image showing the dimming resulting from the eruption. The yellow box marks the coronal dimming indicative of a coronal mass ejection (CME) eruption, while the red cross indicates the projected propagation direction of the CME apex inferred via the GCS technique.
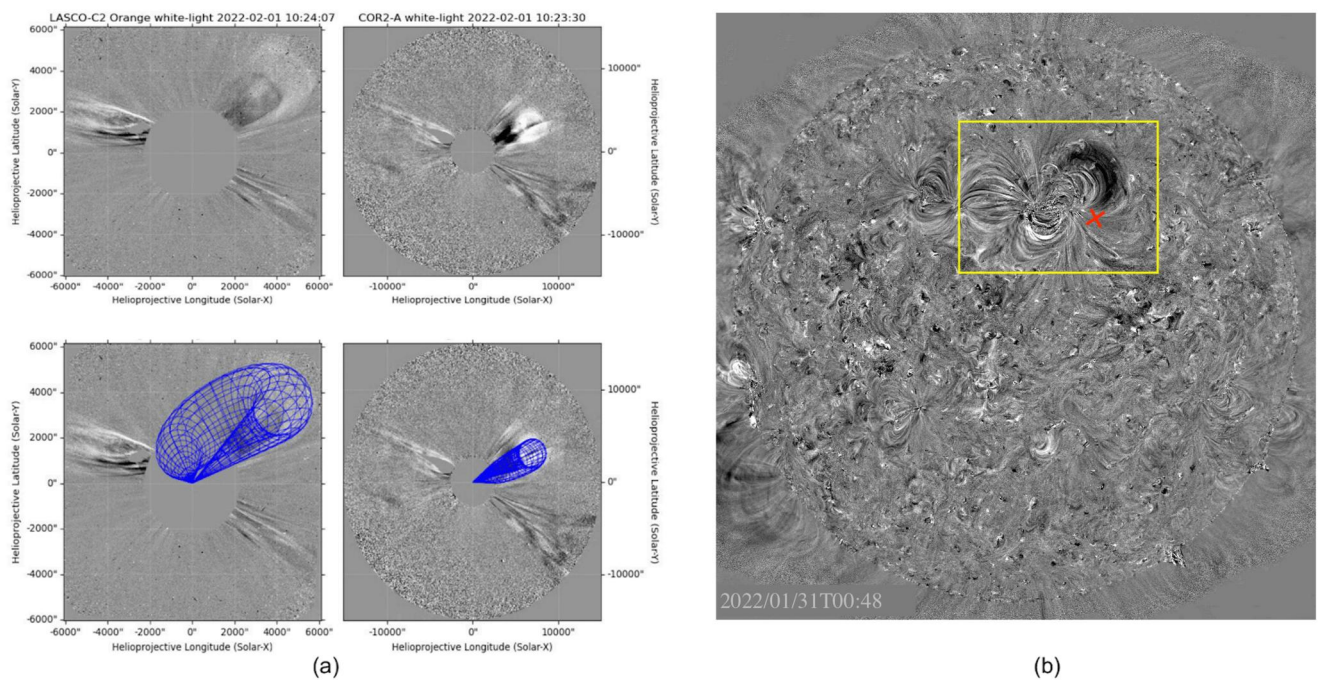

Figure 3. Remote-sensing observations of CME3. (a) The appearance of CME3 in LASCO C2 and STEREO-A COR2 field of view is depicted in the top row and the bottom row describes the fitted Graduated Cylindrical Shell (GCS) flux rope structures on the coronagraph images. (b) A difference image obtained from the STEREO/EUVI-A 171 Å and 195 Å channels. The yellow box indicates an erupting coronal loop as the source signature for the eruption. The red cross indicates the estimated coronal mass ejection source location inferred from the GCS fitting.
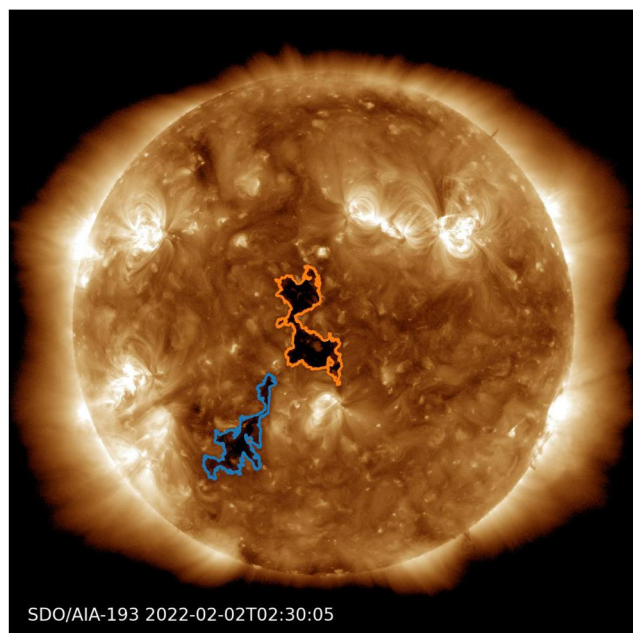
Figure 4. The presence of two coronal holes observed by the SDO/AIA 193 Å channel on 2 February 2022 is marked with orange and blue contours. The high-speed wind coming out of the coronal hole close to the solar equator (marked in orange) is likely to have increased the speed of the observed coronal mass ejections (CMEs), resulting in significant reduction in the CME travel times relative to estimates based on near-Sun kinematics.

In fact two coronal holes, shown in Figure 4, were also observed on the visible solar disk at the time of these eruptions. Streams of fast solar wind emanating from these regions, especially from the equatorial coronal hole (outlined in orange in Figure 4)—could have expedited the propagation of the CMEs, resulting in earlier-than-expected Earth arrivals. It is well known that the push "from behind" exerted by a HSS can result in acceleration and compression, and sometimes in enhanced geoeffectiveness, of a preceding CME (e.g., Palmerio et al., 2022; Y. Wang et al., 2016).

3. Near-Earth Observations of the Geomagnetic Storms That Impacted the Starlink Satellites

Figure 5 shows the solar wind properties near Earth observed by the Wind (Ogilvie & Desch, 1997) and Advanced Composition Explorer (ACE; Stone et al., 1998) spacecraft at the Lagrange L1 point, as well as geomagnetic indices (Dst and Kp) during 1–6 February 2022. The space-based data are obtained from the Magnetic Field Investigation (MFI; Lepping et al., 1995) and Solar Wind Experiment (SWE; Ogilvie et al., 1995) instruments on board Wind, and the Electron, Proton, and Alpha Monitor (EPAM; Gold et al., 1998) onboard ACE, while the ground-based data come from the World Data Center for Geomagnetism, Kyoto (Dst) and NOAA's National Centers for Environmental Information (Kp). A sudden enhancement in the magnetic field, plasma, and particle parameters was observed around 21:30 UT on 1 February, indicating the arrival of the shock driven by CME1 at L1 ("S1" in Figure 5). It was followed by a turbulent sheath region, characterized by high magnetic field, density, and temperature fluctuations, succeeded by a smooth rotation of the magnetic field components denoting a flux rope (Burlaga et al., 1981; Lepping et al., 1990). This flux rope-like ejecta arrived at L1 between 15:30 UT on 2 February and 10:30 UT on 3 February ("E1" in Figure 5). The increasing speed and high temperature within the flux rope suggest that it was compressed by a trailing solar wind HSS that arrived right after the passage of CME1 (e.g., Vandas et al., 2015). The Dst index peaked at a moderate value of −66 nT and the Kp index peaked at 5+ on 3 February due to the impact of CME1.

The Starlink satellites were launched at 18:13 UT on 3 February, about 6 hr after the passage of CME1 at L1, when the near-Earth space environment was still engulfed in the following HSS. Approximately 6 hr after the launch, a second significantly weaker interplanetary shock ("S2" in Figure 5) impacted near-Earth space. The turbulent sheath region downstream of the shock was followed by another ejecta ("E2" in Figure 5), succeeded by signatures of CME–CME interaction ("I23" in Figure 5) with the last ejecta in the series ("E3" in Figure 5). The CME–CME interaction region features irregular magnetic fields as well as elevated temperatures and densities, conforming to the characteristics of "merging CMEs" often described in the literature (e.g., Lugaz & Farrugia, 2014; Palmerio, Nieves-Chinchilla, et al., 2021; Y. M. Wang et al., 2003). We attribute the entire structure (shock–sheath–merged ejecta) to the interacting CME2 and CME3. The merged ejecta is also followed by a CME–HSS interaction structure ("H2" in Figure 5) and again by the HSS, suggesting that the complex ICMEs were fully embedded in the fast solar wind—a feature that is not particularly common but has nevertheless been reported in existing studies (e.g., Heinemann et al., 2019; Palmerio et al., 2023). The Dst index on 4 February peaked at a moderate value of −56 nT in response to the arrival of the CME2 ejecta and further enhanced to −62 nT upon the arrival of CME3. The Kp index peaked at 5+ approximately in between the two dips in the Dst index.

It is noteworthy that both geomagnetic storms could be classified as moderate according to, for example, Loewe and Prölss (1997), and not extreme by any standards.

4. Modeling the Storm-Impacted Magnetosphere

Joule heating resulting from space weather conditions during solar storms, manifests in the thermosphere and ionosphere layers of Earth's atmosphere. Typically, these upper atmospheric regions are heated by two primary
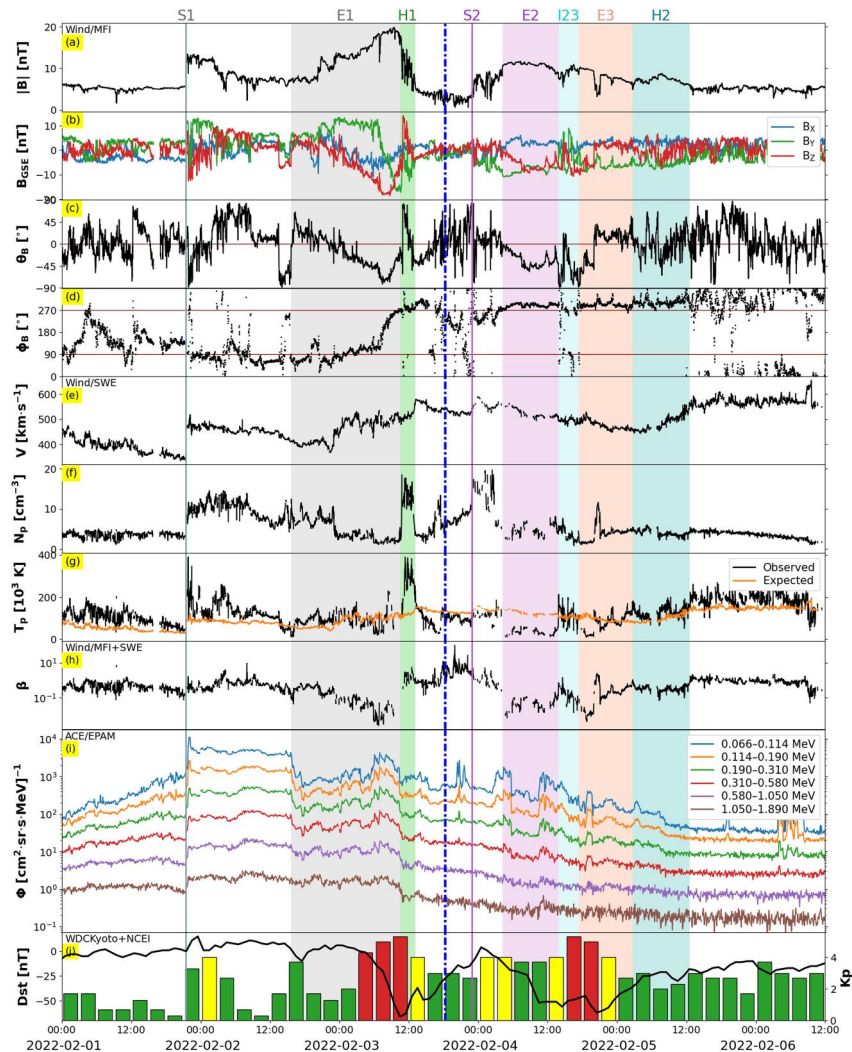
Figure 5. Solar wind conditions observed at L1 by the Wind and ACE spacecraft during February 1–6, 2022. (a) Total magnetic field magnitude. (b) Magnetic field components in the Geocentric Solar Ecliptic coordinate system. (c) Elevation (θ) and (d) azimuthal (ϕ) components of the magnetic field. (e) Solar wind speed. (f) Proton density. (g) Proton temperature. (h) Plasma β. (i) Suprathermal ion fluxes. (j) Geomagnetic indices (Dst and Kp). The expected temperature in (g) is calculated according to Richardson and Cane (1995). Vertical lines and shaded regions indicate the various structures identified in the data, where "S" is used for interplanetary shocks, "E" for ICME ejecta, "H" for CME–HSS interaction regions, and "I" for CME–CME interaction regions. The blue dash-dotted line marks the launch time of the Starlink satellites.

mechanisms: energetic particle precipitation and Joule heating. Under quiet-time circumstances, these two processes tend to be of similar magnitude, but during geomagnetic storms, Joule heating dominates (for detailed understanding, refer to Chappell et al., 2016). The process of atmospheric Joule heating entails the conversion of kinetic energy into thermal energy through collisions between moving charged particles and relatively stationary neutral gas molecules. The cumulative impact of this frictional heating across all particle types, along with the subsequent transfer of heat from warmer to cooler areas, contributes to the overall heating in the thermosphere (see Richmond, 2021; Vasyliūnas & Song, 2005, and references therein). Owing to a higher concentration of neutral species in the thermosphere relative to charged particles, a majority of the Joule heating energy ultimately raises the temperature of the atmosphere, leading to an expansion of the gas density scale height. We note that there are other processes in the ionosphere which may also contribute to storm time response, such as increased ionization, changes in charged particle density in different ionospheric layers in different latitudes due to top-down response to a storm impact, the "Dusk Effect," etc (for a detailed understanding see Buonsanto (1999)
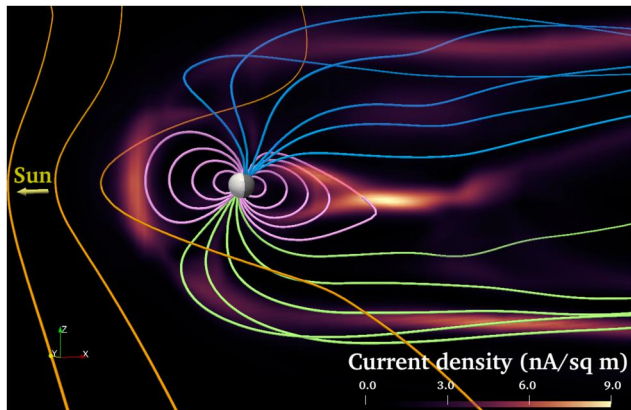
Figure 6. The impact of CME1 on Earth's space environment on 3 February 2022 at 02:25 UT as modeled by the STORMI module. The perturbed geomagnetic field lines are depicted in multi-colored lines while the background color depicts the enhanced current density due to the impact of the storm.

and references therein). In this study we primarily focus on the impact of geomagnetic storm induced Joule heating, consequent neutral density changes in the upper atmosphere and its impact on satellite drag.

To establish this causal link between the identified solar magnetic storms and their impact, we utilize data-driven simulations employing the CESSI Storm Interaction (hereafter STORMI) module (Roy & Nandy, 2023). This module has evolved from the CESSI Star Planet Interaction Module (SPIM; Bharati Das et al., 2019), which employs a 3D compressible resistive MHD framework provided by PLUTO (Mignone et al., 2007) to solve the geospace physics under forcing of solar wind and ICMEs. Within the STORMI module, we simulate the interactions between the three-dimensional magnetic flux rope structures of the observed solar storms, based on in-situ measurements at the Lagrange point L1 (refer to Figure 6), and Earth's magnetosphere. This simulation brings out the physical processes that occur during the interaction of solar transients with the Earth's magnetosphere.

The Birkeland currents, also referred to as the field-aligned currents, are always present in the auroral regions. They propagate along the magnetic field lines and play a vital role in connecting the magnetosphere to the ionosphere (Potemra, 1994). Most importantly, their strength varies significantly in response to changes in geomagnetic activity, as noted by Anderson et al. (1993). Within the ionosphere, horizontal Pedersen currents link these field-aligned currents, forming a closed loop for the flow of electric charge. Since it's the Pedersen currents that are known to mainly lead to the Joule heating of the upper atmosphere, studies have often used Birkeland field-aligned currents as a proxy estimate of the Pedersen current to measure the Joule heating (Anderson et al., 1998).

We adopt a similar approach by utilizing the induced current density data acquired from the STORMI module surrounding Earth to make a qualitative assessment of Joule heating. We compute both the total induced current, denoted as J, and the field-aligned current, designated as $J_{\parallel}$, which aligns parallel to the local magnetic field vector at each grid point. Our calculation involves determining the average value of the squares of these induced currents, denoted as $\langle J^2 \rangle$ and $\langle J_{\parallel}^2 \rangle$, over the volume of a geocentric sphere with a radius of 8 R_E within the magnetosphere, where R_E is the radius of Earth. These estimations, though qualitative in nature, offer a good approximation of the overarching manifestation of Joule heating within our modeled magnetospheric environment.

We observe a remarkable surge of nearly 329% in $\langle J_{\parallel}^2 \rangle$ and an even more substantial increase of around 628% in $\langle J^2 \rangle$ from the respective global average values across the simulated magnetospheric region in response to the geomagnetic storm triggered by CME1 on 3 February 2022. Subsequently, there is another significant increase of around 290% in $\langle J^2 \rangle$ and a notable 190% increase in $\langle J_{\parallel}^2 \rangle$ due to the combined impact of CME2 and CME3 on 4 February. These findings are illustrated in the top row of Figure 7.

As an independent verification measure, we utilize the Space Weather Modeling Framework's Block Adaptive Tree Solar wind Roe-type Upwind Scheme code (SWMF/BAT-S-RUS; Gombosi et al., 2021; Tóth et al., 2012, 2005) through the NASA Community Coordinated Modeling Center (CCMC). This allows us to calculate the average of both the square of total induced currents ($\langle J^2 \rangle$) and field-aligned currents $\left(\langle J_{\parallel}^2 \rangle \right)$ within the same magnetospheric volume, serving as a validation of the reliability of our findings obtained from the STORMI module.

As we compare the global temporal profiles of current densities from SWMF with those derived from STORMI, a notable and robust correlation emerges, as illustrated in panels (a) and (b) of Figure 8, with a Pearson's coefficient of 0.82 for both comparisons. Furthermore, the ionospheric Joule heating data obtained from SWMF closely aligns the profile of $\langle J_{\parallel}^2 \rangle$ derived from STORMI, demonstrating a particularly strong resemblance with a Pearson's coefficient of 0.90, as depicted in panel (c) of Figure 8. This alignment reinforces our hypothesis that utilizing the induced currents from our simulation as a proxy for Joule heating is a valid and well-founded approximation.
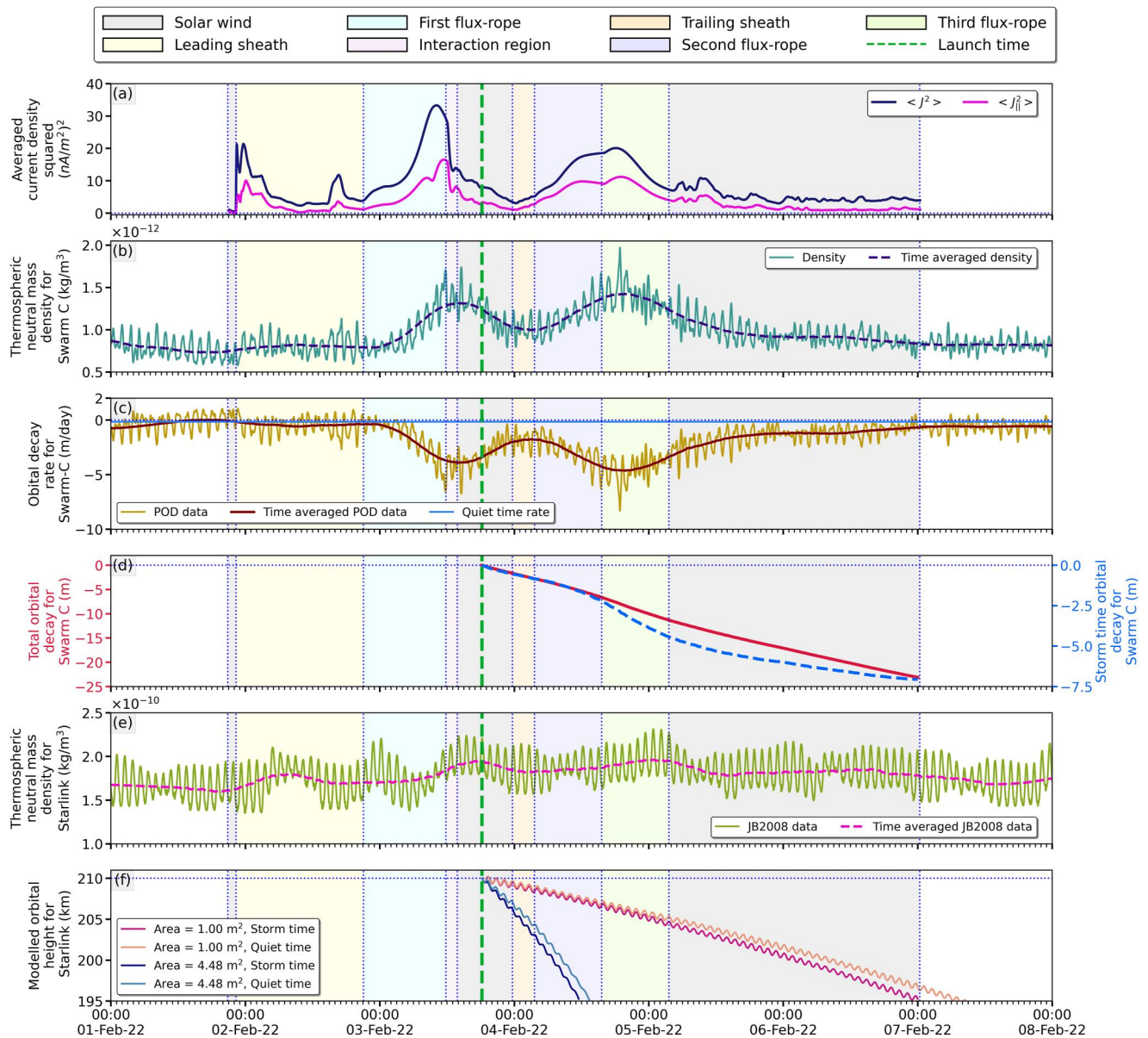
Figure 7. (a) Averaged J^2 and $J_\parallel^2$ variation for a geocentric sphere of radius 8 R_E. (b) The thermospheric neutral mass density variation at the altitude of the Swarm C satellite, derived from accelerometer data and made available at https://swarm-diss.eo.esa.int/. (c) Estimated orbital decay rate for Swarm C due to the geomagnetic storm (maroon) with the quiet, non-storm time, decay rate (blue). (d) The Swarm C orbital decay (blue) induced by the geomagnetic storm is marked on the right vertical axis and the total orbital decay (red) values including the background contribution is marked on the left vertical axis. (e) The thermospheric neutral mass density variation at the altitude of the Starlink satellites obtained from the JB2008 model. (f) Total modeled orbital decay of the Starlink satellites for likely minimum and maximum ram areas (1.00 and 4.48 m²), with estimated quiet time decay shown for comparison. The colored backgrounds indicating different in-situ structures are shifted forward in time with respect to the solar wind measurements in Figure 5 to account for the passage time of magnetic transients from the Lagrange L1 point to Earth. The time of launch of the Starlink satellites is indicated by the green vertical dashed line.

Nevertheless, our study from the physics-driven simulations conducted by STORMI, bolstered by corroborating simulations from SWMF, reveal that the region near Earth experienced physical perturbations directly linked to the solar transients that occurred concurrently with the deployment of the Starlink satellites. We now complement these modeling results of perturbations in the near-Earth space environment with independent observations and empirical models of atmospheric drag enhancement and resultant satellite orbital decay concurrent with the timing of the loss of the Starlink satellites.
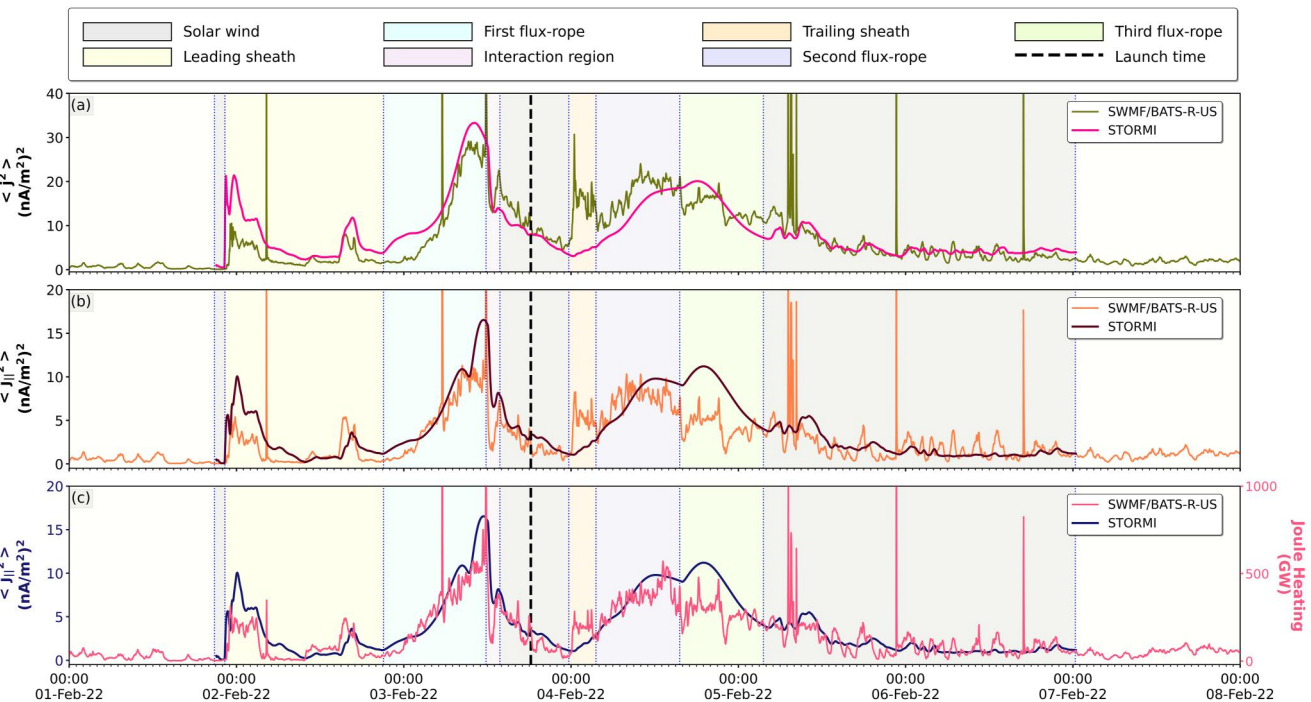
Figure 8. The panels illustrate the correlation between the outcomes derived from SWMF/BATSRUS and STORMI. Panel (a) and (b) demonstrate the temporal profile similarity of $\langle J^2 \rangle$ and $\langle J_{\parallel}^2 \rangle$, respectively. In panel (c), the Ionospheric Joule heating from SWMF/BATSRUS and $\langle J_{\parallel}^2 \rangle$ are plotted side by side, using parallel and color-coded y-axis to visually highlight the qualitative resemblance.

5. Empirical Modeling of Orbital Decay of the Starlink Satellites

We use Precise Orbit Determination (POD) data from the ESA Swarm C satellite (Olsen et al., 2013), located at approximately 434 km, and satellite orbit simulations to study the impact of the geomagnetic storms on satellite altitude (as outlined by Chen et al., 2012). The uncertainty in the Swarm C drag acceleration is $\sim 10^{-7}$ m/s^2 in the satellite's in-track direction (Siemes et al., 2016). Since this calculation is performed for comparison to the orbital decay of the Starlink satellites, we did not attempt to compute the drag coefficient C_D for the Swarm C satellite and assumed it to be unity (which suffices for a comparative analysis). The thermospheric density in the orbit of Swarm C steeply increased by 125% on 3 February and by 156% on 4 February relative to quiet days due to the corresponding geomagnetic storms that occurred on these days (Figure 7). Our analysis of thermopsheric density enhancements during the loss of the Starlink satellites is consistent with previous studies on the event which have suggested significant atmospheric disturbance on 3 and 4 February 2022. In Table S1 (Supporting Information S1) we provide a comprehensive list of thermospheric density enhancements during this epoch gleaned from previous studies; while there are quantitative variations in individual estimates all studies qualitatively agree on significant thermospheric density perturbations concurrent with the loss of the Starlink satellites. A maximum increase in orbital decay rate of Swarm C by 32.5 times the quiet time decay rate is observed following the geomagnetic storm of 3 February (Figure 7). The second storm that occurred on 4 February spiked up the decay rates yet again by 40 times in comparison to quiet time values. The total orbital decay for the Swarm C satellite (Figure 7) from the launch time of the Starlink satellites to 6 February 2022 was 23.08 m (for $C_D = 1$; it will be proportionately higher for higher C_D).

To relatively estimate the orbital decay of the Starlink satellites, we create 2-D synthetic orbits. The local thermospheric density used in the calculations has been estimated using the Jacchia-Bowman (JB2008) model (Bowman et al., 2008). It is well known that thermospheric empirical models can be subjected to significant errors when computing atmospheric mass densities during geomagnetic storms (He et al., 2018). However, such errors become significantly high during intense and extreme geomagnetic storms. For example, densities computed by JB2008 can show errors of up to 35% during extreme geomagnetic storms (Bowman et al., 2008; Oliveira et al., 2021; Oliveira & Zesta, 2019). A recently identified source of errors in density and orbital decay

computations by empirical models is the enhancement of nitric oxide (NO) molecules, a cooling agent in the upper atmosphere that radiates heat back to space (Knipp et al., 2017; Mlynczak et al., 2003). Such effects are more pronounced during the recovery phase of extreme geomagnetic storms (Oliveira et al., 2021; Oliveira & Zesta, 2019; Zesta & Oliveira, 2019), which did not occur in February 2022. On the other hand, as shown by Bowman et al. (2008), density errors during moderate storms, such as the one analyzed in this study, are on average 15%, which is significantly lower. Therefore, eventual errors introduced by JB2008 in our results have low to moderate impacts in our conclusions, at least in comparison to extreme geomagnetic storms.

The orbital decay of Swarm C, using the synthetic ephemeris, from the time of launch of the Starlink satellites to 6 February was obtained to be 25.02 m. This is in good agreement with the observed values. We then extend these calculations for the Starlink satellites in the same time frame, which were launched to an orbit of 210 km altitude at an inclination of 53.22°, considering two cross-sectional areas: 1.00 and 4.48 m^2, and C_D to be unity. The satellite ram areas are representative of the expected range of cross-sectional areas based on the geometry and assumed open book and shark fin configurations respectively of the Starlink satellites. Relative to quiet times, the prevailing geomagnetic storms are estimated to result in a faster orbital decay of the Starlink satellites by 6 hr for a ram surface area of 1.00 m^2. The corresponding decay time is 2 hr faster with respect to quiet time conditions assuming a ram area of 4.48 m^2 (Figure 7).

Furthermore, for a ram surface area of 4.48 m^2 (1.00 m^2) our calculations indicate that the Starlink satellites would have decayed to a (near) "unrecoverable" altitude of 100.01 km (203.24 km) by 08:58 UT on 5 February. It is noteworthy that SpaceX announced the Starlink satellites to have been "significantly impacted" by a geomagnetic storm on 4 February itself (https://www.spacex.com/updates/). This suggests that the doomed satellites—on multiple instances—might have assumed orientations that exposed a larger ram area to the storm-perturbed atmosphere immediately after orbital insertion, tipping them beyond the point of recovery.

Dang et al. (2022) have also reported thermospheric density observations from Swarm C satellite and simulated orbital decay of the Starlink satellites for different cross-sectional areas. However, our study computes the orbital decay of Swarm C satellite as well in addition to reporting the thermospheric density at the altitude of Swarm C during the period of scrutiny. This analysis of Swarm C is used to validate our empirical model for satellite orbital decay before applying it to the Starlink satellites.

5.1. Comparative Analysis of the Starlink and Swarm C Orbital Decay

We perform a comparative analysis of the impact of the enhanced thermospheric density at 210 and 434 km on both the Starlink and Swarm C satellites. To achieve this, we hypothetically place the Swarm C satellite at the Starlink altitude and correspondingly hypothetically place the Starlink satellite (with ram areas 1.00 and 4.48 m^2) at the Swarm C altitude via generation of a synthetic ephemeris (Figure 9). Our calculations demonstrate that the Starlink satellites suffer an altitude decay that is about 3 times higher than Swarm C in both instances, suggesting that the amount of orbital decay a satellite undergoes is influenced by the design of the spacecraft.

This enhanced decay could be attributed to the low ballistic coefficient (low mass-to-area ratio) of the Starlink satellites relative to Swarm C, denoted by the term $\frac{m}{C_D A}$ (de Lafontaine & Garg, 1982). The lower the ballistic coefficient (lower the mass-to-area ratio), higher is the impact of drag on the motion of the body. The ballistic coefficient of Swarm C ($C_D = 1$), having a mass of about 468 kg and ram area of 0.7 m^2, is approximately 3 times higher than that of a Starlink satellite ($C_D = 1$), which has a mass of 227 kg, even for the minimum cross-sectional area of 1.00 m^2. Additionally, our conclusions would still hold even if we considered C_D errors of up to ~20% (Sutton, 2009). This indicates that Starlink satellites have attributes that may have subjected them to enhanced atmospheric drag forces relative to the Swarm C satellite. This study shows that in addition to a low-altitude insertion, the low ballistic coefficient of the Starlink satellites may have further compromised their ability to recover from the impact of the Sun-induced geomagnetic storms.

6. Discussion and Conclusions

In this work, we have analyzed the solar sources of the moderate magnetic storms concurrent with the loss of the Starlink satellites in February 2022. We have identified their physical properties and used these as inputs to drive physics-based magnetohydrodynamic models to explore space weather induced perturbations in the near-Earth space environment that were experienced by the Starlink satellites. Our modeling indicates that the satellites
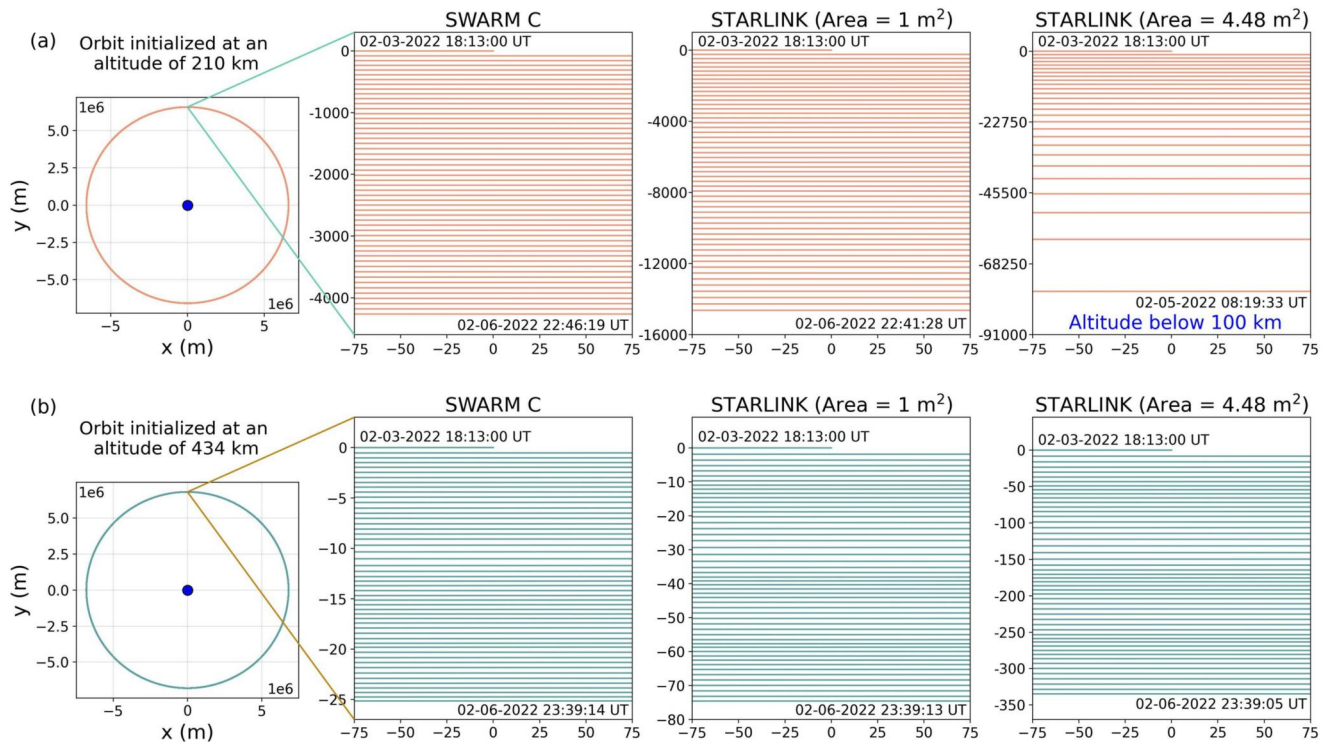
Figure 9. Panels (a) and (b) depict reconstructed orbits initialized at 210 km (Starlink insertion altitude) and 434 km (Swarm C altitude), respectively on 3 February 2022 at 18:13 UT. The left-most panels in (a) and (b) represent the global view of the orbits with the blue dot representing Earth's center. The vertical axis of the figure, $y(m)$, denotes the orbital altitude of the satellite. The horizontal axis, $x(m)$, is the distance of the satellite from the center of the orbit perpendicular to y. The second panels from the left depict zoomed-in views of the orbital passes of the Swarm C satellite at a representative rectangular cross-section. The third and fourth panels from the left show corresponding orbital passes of the Starlink satellites with assumed ram areas of 1 and 4.48 m². The time corresponding to the first and last orbital passes, respectively, are mentioned at the top and bottom of the second, third and fourth panels from the left. The drag coefficient for both the satellites in this analysis is taken to be unity.

were launched into a moderately perturbed space environment which persisted over many days. We note that we have used two disparate approaches in this study, one based on data-driven magnetohydrodynamic simulations of current density enhancements in the near-Earth space environment (with the STORMI module) and another based on empirical estimates of thermospheric density enhancements (based on the JB2008 model). The fact that physically modeled current density enhancements are found to be roughly concurrent with independent empirical estimates of density enhancements, reinforces the conclusion that the LEO where the doomed Starlink satellites were injected, were indeed subjected to solar induced perturbations. Independent investigations of atmospheric drag enhancement and resultant orbital decay, relying on observations and empirical models, confirm that the Starlink satellites faced enhanced drag at their orbit of insertion due to the perturbed space environment. We thus establish causality between the solar sources of space weather perturbations and their impact at LEO.

We reach the surprising conclusion that even moderate space weather events can conspire together with low-altitude orbital insertions and physical properties of satellites to bring about catastrophic losses. We note that severe space weather can further compound such hazards by leading to loss of telemetry, orbital positional knowledge and an uncontrolled re-orientation of satellites. The design and operation of spacecraft meant for LEO insertion must therefore take cognizance of these cumulative effects for operational mission planning. This includes space weather awareness and availability of relatively high-thrust propulsion systems that can rapidly raise satellite altitudes to a region of lower density and thus lower drag when they encounter geomagnetic storms.

We note that 11 of the 49 Starlink satellites that were launched on 3 February survived the low altitude insertion during the perturbed space weather conditions. Anisotropic thermospheric density variations may have subjected individual satellites to different drag forces based on their precise orbit of injection and location (Fang et al., 2022; Lin et al., 2022). Some satellites may have been favourably oriented presenting a lower ram area and thus reduced drag. We surmise that these two possibilities, in isolation or in tandem, could have resulted in the survival of the 11 satellites.

Nonetheless, with humanity's ever-increasing dependence on LEO satellites for communication, navigation, geospatial imaging, defense, and disaster management systems, our findings call for closer synergy and inter-disciplinary knowledge exchange between space agencies, private satellite operators, satellite engineers, and heliophysics domain experts including solar physicists, ionospheric physicists, and atmospheric physicists—in order to fully appreciate and mitigate the impacts of our space environment on human technologies.

Data Availability Statement

SOHO LASCO coronagraph data used in this study can be accessed from the Virtual Solar Observatory (Hill et al., 2009) by selecting SOHO/LASCO from the list of Source/Instrument for the duration of 29 January 2022, 00:00 UT to 1 Feb 2022, 23:59 UT. STEREO-A COR 2 and EUVI data were obtained from the STEREO Science Center data archive (Kaiser et al., 2008). SDO AIA Level 1 data of 12s cadence, from 29 January 2022 to 1 February 2022, used for solar source identification have been obtained from the Joint Science Operations Center (Hapgood et al., 1997). The solar wind in-situ data from 1 February to 6 February 2022 are provided by the Wind (Koval & Szabo, 2021) and ACE spacecraft (Smith & Ness, 2022), and geomagnetic indices are provided by the WDC Kyoto (Nose et al., 2015) and NOAA's NCEI via OMNI (King & Papitashvili, 2005), all accessible at NASA's CDAWeb. We have used the SunPy (SunPy Community et al., 2020) package for analysis of data and the JHelioviewer (Müller et al., 2017) software for visualization of solar data. Level2daily POD data and Level2daily local thermospheric density data was used for satellite drag calculations for Swarm C (Olsen et al., 2013). Refer to Baruah et al. (2023) for the simulated current density from the STORMI and SWMF/BATSRUS modules, as well as the Joule heating estimated using the SWMF/BATSRUS tools. Anyone utilizing the data should cite this work, along with other relevant publications associated with the SWMF/BATSRUS models.

References

Anderson, B. J., Gary, J. B., Potemra, T. A., Frahm, R. A., Sharber, J. R., & Winningham, J. D. (1998). UARS observations of Birkeland currents and Joule heating rates for the November 4, 1993, storm. *Journal of Geophysical Research*, *103*(A11), 26323–26336. https://doi.org/10.1029/98JA01236

Anderson, B. J., Potemra, T. A., Bythrow, P. F., Zanetti, L. J., Holland, D. B., & Winningham, J. D. (1993). Auroral currents during the magnetic storm of November 8 and 9, 1991: Observations from the upper atmosphere research satellite particle environment monitor. *Geophysical Research Letters*, *20*(12), 1327–1330. https://doi.org/10.1029/93GL01106

Barnes, W. T., Barnes, W. T., Bobra, M. G., Christe, S. D., Freij, N., Hayes, L. A., et al. (2020). The SunPy project: Open source development and status of the version 1.0 core package [Software]. The Astrophysical Journal, *890*(1), 68. https://doi.org/10.3847/1538-4357/ab4f7a

Baruah, Y., Roy, S., Sinha, S., Palmerio, E., Pal, S., Oliveira, D. M., & Nandy, D. (2023). The loss of the Starlink satellites in February 2022: How moderate geomagnetic storms can adversely affect assets in Low-Earth Orbit [Dataset]. Zenodo. https://doi.org/10.5281/ZENODO.8331135

Berger, T. E., Dominique, M., Lucas, G., Pilinski, M., Ray, V., Sewell, R., et al. (2023). The thermosphere is a drag: The 2022 Starlink incident and the threat of geomagnetic storms to low earth orbit space operations. *Space Weather*, *21*(3), e2022SW003330. https://doi.org/10.1029/2022SW003330

Bharati Das, S., Basak, A., Nandy, D., & Vaidya, B. (2019). Modeling star-planet interactions in far-out planetary and exoplanetary systems. *The Astrophysical Journal*, *877*(2), 80. https://doi.org/10.3847/1538-4357/ab18ad

Bowman, B. R., Tobiska, W. K., Marcos, F. A., Huang, C. Y., Lin, C. S., & Burke, W. J. (2008). A new empirical thermospheric density model JB2008 using new solar and geomagnetic indices. In *Aiaa/aas astrodynamics specialist conference* (p. 6438).

Brueckner, G. E., Howard, R. A., Koomen, M. J., Korendyke, C. M., Michels, D. J., Moses, J. D., et al. (1995). The large angle spectroscopic coronagraph (LASCO). *Solar Physics*, *162*(1–2), 357–402. https://doi.org/10.1007/BF00733434

Buonsanto, M. J. (1999). Ionospheric storms—A review. *Space Science Reviews*, *88*(3–4), 563–601. https://doi.org/10.1023/a:1005107532631

Burlaga, L., Sittler, E., Mariani, F., & Schwenn, R. (1981). Magnetic loop behind an interplanetary shock: Voyager, Helios, and IMP 8 observations. *Journal of Geophysical Research*, *86*(A8), 6673–6684. https://doi.org/10.1029/JA086iA08p06673

Čalogović, J., Dumbović, M., Sudar, D., Vršnak, B., Martinić, K., Temmer, M., & Veronig, A. M. (2021). Probabilistic drag-based ensemble model (DBEM) evaluation for heliospheric propagation of CMEs. *Solar Physics*, *296*(7), 114. https://doi.org/10.1007/s11207-021-01859-5

Chappell, C. R., Schunk, R. W., Banks, P. M., Burch, J. L., & Thorne, R. M. (2016). Magnetosphere-ionosphere coupling in the solar system. https://doi.org/10.1002/9781119066880

Chen, G.-M., Xu, J., Wang, W., Lei, J., & Burns, A. G. (2012). A comparison of the effects of CIR- and CME-induced geomagnetic activity on thermospheric densities and spacecraft orbits: Case studies. *Journal of Geophysical Research*, *117*(A8), A08315. https://doi.org/10.1029/2012JA017782

Dang, T., Li, X., Luo, B., Li, R., Zhang, B., Pham, K., et al. (2022). Unveiling the space weather during the Starlink satellites destruction event on 4 February 2022. *Space Weather*, *20*(8), e2022SW003152. https://doi.org/10.1029/2022SW003152

de Lafontaine, J., & Garg, S. C. (1982). A review of satellite lifetime and orbit decay prediction. *Proceedings of the Indian Academy of Sciences - Section A*, *5*(3), 197–258. https://doi.org/10.1007/bf02897683

Domingo, V., Fleck, B., & Poland, A. I. (1995). The SOHO mission: An overview. *Solar Physics*, *162*(1–2), 1–37. https://doi.org/10.1007/BF00733425

Duann, Y., Chang, L. C., & Liu, J.-Y. (2023). Impact of the February 3-4, 2022 geomagnetic storm on ionospheric S4 amplitude scintillation index: Observations and implications. *Advances in Space Research*, *72*(10), 4379–4391. https://doi.org/10.1016/j.asr.2023.09.036

Fang, T.-W., Kubaryk, A., Goldstein, D., Li, Z., Fuller-Rowell, T., Millward, G., et al. (2022). Space weather environment during the SpaceX Starlink satellite loss in February 2022. *Space Weather*, *20*(11), e2022SW003193. https://doi.org/10.1029/2022SW003193

Gold, R. E., Krimigis, S. M., Hawkins, S., Haggerty, D. K., Lohr, D. A., Fiore, E., et al. (1998). Electron, proton, and Alpha monitor on the advanced composition explorer spacecraft. *Space Science Reviews*, *86*(1/4), 541–562. https://doi.org/10.1023/A:1005088115759

Gombosi, T. I., Chen, Y., Glocer, A., Huang, Z., Jia, X., Liemohn, M. W., et al. (2021). What sustained multi-disciplinary research can achieve: The space weather modeling framework. *Journal of Space Weather and Space Climate*, *11*, 42. https://doi.org/10.1051/swsc/2021020

Gopalswamy, N., Xie, H., Yashiro, S., & Akiyama, S. (2023). The solar cause of the 2022 February 3 geomagnetic storm that led to the demise of the Starlink satellites. *Sun Geosphere*, *15*, 65–74. https://doi.org/10.31401/SunGeo.2022.02.04

Gosling, J. T., McComas, D. J., Phillips, J. L., & Bame, S. J. (1991). Geomagnetic activity associated with Earth passage of interplanetary shock disturbances and coronal mass ejections. *Journal of Geophysical Research*, *96*(A5), 7831–7839. https://doi.org/10.1029/91JA00316

Guarnieri, F. L., Tsurutani, B. T., Hajra, R., Echer, E., & Lakhina, G. S. (2023). NORAD tracking of the February 2022 Starlink satellites (and the possible immediate loss of 32 satellites). arXiv e-prints, arXiv:2307.02923. https://doi.org/10.48550/arXiv.2307.02923

Gulyaeva, T., Lukianova, R., & Haralambous, H. (2023). Ionosphere heterogeneities at Dawn−Dusk terminator related to the Starlink satellites launch disaster on 3−8 February 2022. *Journal of Geophysical Research: Space Physics*, *128*(11), e2023JA031577. https://doi.org/10.1029/2023JA031577

Hapgood, M., Dimbylow, T., Sutcliffe, D., Chaizy, P., Ferron, P., Hill, P., & Tiratay, X. (1997). The joint science operations centre. *Space Science Reviews*, *79*(1–2), 487–525. https://doi.org/10.1023/a:1004954504114

Hapgood, M., Liu, H., & Lugaz, N. (2022). SpaceX—Sailing close to the space weather? *Space Weather*, *20*(3), e2022SW003074. https://doi.org/10.1029/2022SW003074

He, C., Yang, Y., Carter, B., Kerr, E., Wu, S., Deleflie, F., et al. (2018). Review and comparison of empirical thermospheric mass density models. *Progress in Aerospace Sciences*, *103*, 31–51. https://doi.org/10.1016/j.paerosci.2018.10.003

He, J., Astafyeva, E., Yue, X., Pedatella, N. M., Lin, D., Fuller-Rowell, T. J., et al. (2023). Comparison of empirical and theoretical models of the thermospheric density enhancement during the 3–4 February 2022 geomagnetic storm. *Space Weather*, *21*(9). e2023SW003521. https://doi.org/10.1029/2023SW003521

Heinemann, S. G., Temmer, M., Farrugia, C. J., Dissauer, K., Kay, C., Wiegelmann, T., et al. (2019). CME-HSS interaction and characteristics tracked from Sun to Earth. *Solar Physics*, *294*(9), 121. https://doi.org/10.1007/s11207-019-1515-6

Hill, F., Martens, P., Yoshimura, K., Gurman, J., Hourclé, J., Dimitoglou, G., et al. (2009). The virtual solar observatory—A resource for international heliophysics research. *Earth, Moon, and Planets*, *104*(1–4), 315–330. https://doi.org/10.1007/s11038-008-9274-7

Howard, R. A., Moses, J. D., Vourlidas, A., Newmark, J. S., Socker, D. G., Plunkett, S. P., et al. (2008). Sun Earth connection coronal and heliospheric investigation (SECCHI). *Space Science Reviews*, *136*(1–4), 67–115. https://doi.org/10.1007/s11214-008-9341-4

Jin, M., Cheung, M. C. M., DeRosa, M. L., Nitta, N. V., & Schrijver, C. J. (2022). Coronal mass ejections and dimmings: A comparative study using MHD simulations and SDO observations. *The Astrophysical Journal*, *928*(2), 154. https://doi.org/10.3847/1538-4357/ac589b

Kaiser, M. L., Kucera, T. A., Davila, J. M., Cyr, O. C., St., Guhathakurta, M., & Christian, E. (2008). The STEREO mission: An introduction. *Space Science Reviews*, *136*(1–4), 5–16. https://doi.org/10.1007/s11214-007-9277-0

Kataoka, R., Shiota, D., Fujiwara, H., Jin, H., Tao, C., Shinagawa, H., & Miyoshi, Y. (2022). Unexpected space weather causing the reentry of 38 Starlink satellites in February 2022. *Journal of Space Weather and Space Climate*, *12*, 41. https://doi.org/10.1051/swsc/2022034

King, J. H., & Papitashvili, N. E. (2005). Solar wind spatial scales in and comparisons of hourly wind and ace plasma and magnetic field data. *Journal of Geophysical Research*, *110*(A2), A02104. https://doi.org/10.1029/2004ja010649

Knipp, D. J., Pette, D. V., Kilcommons, L. M., Isaacs, T. L., Cruz, A. A., Mlynczak, M. G., et al. (2017). Thermospheric nitric oxide response to shock-led storms. *Space Weather*, *15*(2), 325–342. https://doi.org/10.1002/2016SW001567

Knipp, D. J., Tobiska, W. K., & Emery, B. A. (2004). Direct and indirect thermospheric heating sources for solar cycles 21-23. *Solar Physics*, *224*(1–2), 495–505. https://doi.org/10.1007/s11207-005-6393-4

Koval, A., & Szabo, A. (2021). Wind magnetic field investigation (mfi) data at full resolution [Dataset]. NASA Space Physics Data Facility. https://doi.org/10.48322/0V0H-DF27

Laskar, F. I., Sutton, E. K., Lin, D., Greer, K. R., Aryal, S., Cai, X., et al. (2023). Thermospheric temperature and density variability during 3-4 February 2022 minor geomagnetic storm. *Space Weather*, *21*(4), e2022SW003349. https://doi.org/10.1029/2022SW003349

Lemen, J. R., Title, A. M., Akin, D. J., Boerner, P. F., Chou, C., Drake, J. F., et al. (2012). The atmospheric imaging assembly (AIA) on the solar dynamics observatory (SDO). *Solar Physics*, *275*(1–2), 17–40. https://doi.org/10.1007/s11207-011-9776-8

Lepping, R. P., Acũna, M. H., Burlaga, L. F., Farrell, W. M., Slavin, J. A., Schatten, K. H., et al. (1995). The wind magnetic field investigation. *Space Science Reviews*, *71*(1–4), 207–229. https://doi.org/10.1007/BF00751330

Lepping, R. P., Jones, J. A., & Burlaga, L. F. (1990). Magnetic field structure of interplanetary magnetic clouds at 1 AU. *Journal of Geophysical Research*, *95*(A8), 11957–11965. https://doi.org/10.1029/JA095iA08p11957

Lin, D., Wang, W., Garcia-Sage, K., Yue, J., Merkin, V., McInerney, J. M., et al. (2022). Thermospheric neutral density variation during the "SpaceX" storm: Implications from physics-based whole geospace modeling. *Space Weather*, *20*(12), e2022SW003254. https://doi.org/10.1029/2022SW003254

Lockwood, M., Owens, M. J., & Barnard, L. A. (2023). Universal time variations in the magnetosphere and the effect of CME arrival time: Analysis of the February 2022 event that led to the loss of Starlink satellites. *Journal of Geophysical Research: Space Physics*, *128*(3), e2022JA031177. https://doi.org/10.1029/2022JA031177

Loewe, C. A., & Prölss, G. W. (1997). Classification and mean behavior of magnetic storms. *Journal of Geophysical Research*, *102*(A7), 14209–14214. https://doi.org/10.1029/96JA04020

Lugaz, N., & Farrugia, C. J. (2014). A new class of complex ejecta resulting from the interaction of two CMEs and its expected geoeffectiveness. *Geophysical Research Letters*, *41*(3), 769–776. https://doi.org/10.1002/2013GL058789

Mignone, A., Bodo, G., Massaglia, S., Matsakos, T., Tesileanu, O., Zanni, C., & Ferrari, A. (2007). PLUTO: A numerical code for computational Astrophysics. *The Astrophysical Journal - Supplement Series*, *170*(1), 228–242. https://doi.org/10.1086/513316

Mlynczak, M. G., Martin-Torres, F. J., Russell, J., Beaumont, K., Jacobson, S., Kozyra, J., et al. (2003). The natural thermostat of nitric oxide emission at 5.3 μm in the thermosphere observed during the solar storms of April 2002. *Geophysical Research Letters*, *30*(21). https://doi.org/10.1029/2003GL017693

Müller, D., Nicula, B., Felix, S., Verstringe, F., Bourgoignie, B., Csillaghy, A., et al. (2017). JHelioviewer. Time-dependent 3D visualisation of solar and heliospheric data [Software]. Astronomy and Astrophysics, *606*, A10. https://doi.org/10.1051/0004-6361/201730893

Nandy, D., Baruah, Y., Bhowmik, P., Dash, S., Gupta, S., Hazra, S., et al. (2023). Causality in heliophysics: Magnetic fields as a bridge between the Sun's interior and the Earth's space environment. *Journal of Atmospheric and Solar-Terrestrial Physics*, *248*, 106081. https://doi.org/10.1016/j.jastp.2023.106081

Nitta, N. V., Mulligan, T., Kilpua, E. K. J., Lynch, B. J., Mierla, M., O'Kane, J., et al. (2021). Understanding the origins of problem geomagnetic storms associated with "Stealth" coronal mass ejections. *Space Science Reviews*, *217*(8), 82. https://doi.org/10.1007/s11214-021-00857-0

Nose, M., Sugiura, M., Kamei, T., Iyemori, T., & Koyama, Y. (2015). Dst index [Dataset]. WDC for Geomagnetism, Kyoto. https://doi.org/10.17593/14515-74000

Ogilvie, K. W., Chornay, D. J., Fritzenreiter, R. J., Hunsaker, F., Keller, J., Lobell, J., et al. (1995). SWE, A comprehensive plasma instrument for the wind spacecraft. *Space Science Reviews*, *71*(1–4), 55–77. https://doi.org/10.1007/BF00751326

Ogilvie, K. W., & Desch, M. D. (1997). The wind spacecraft and its early scientific results. *Advances in Space Research*, *20*(4–5), 559–568. https://doi.org/10.1016/S0273-1177(97)00439-0

Oliveira, D. M., & Zesta, E. (2019). Satellite orbital drag during magnetic storms. *Space Weather*, *17*(11), 1510–1533. https://doi.org/10.1029/2019SW002287

Oliveira, D. M., Zesta, E., Mehta, P. M., Licata, R. J., Pilinski, M. D., Kent Tobiska, W., & Hayakawa, H. (2021). The current state and future directions of modeling thermosphere density enhancements during extreme magnetic storms. *Frontiers in Astronomy and Space Sciences*, *8*(764144). https://doi.org/10.3389/fspas.2021.764144

Oliveira, D. M., Zesta, E., Schuck, P. W., & Sutton, E. K. (2017). Thermosphere global time response to geomagnetic storms caused by coronal mass ejections. *Journal of Geophysical Research: Space Physics*, *122*(10), 10762–10782. https://doi.org/10.1002/2017JA024006

Olsen, N., Friis-Christensen, E., Floberghagen, R., Alken, P., Beggan, C. D., Chulliat, A., et al. (2013). The Swarm satellite constellation application and research facility (SCARF) and Swarm data products. *Earth Planets and Space*, *65*(11), 1189–1200. https://doi.org/10.5047/eps.2013.07.001

Pal, S., Balmaceda, L., Weiss, A. J., Nieves-Chinchilla, T., Carcaboso, F., Kilpua, E., & Möstl, C. (2023). Global insight into a complex-structured heliosphere based on the local multi-point analysis. *Frontiers in Astronomy and Space Sciences*, *10*, 1195805. https://doi.org/10.3389/fspas.2023.1195805

Palmerio, E., Lee, C. O., Richardson, I. G., Nieves-Chinchilla, T., Dos Santos, L. F. G., Gruesbeck, J. R., et al. (2022). CME evolution in the structured heliosphere and effects at Earth and Mars during solar minimum. *Space Weather*, *20*(9). e2022SW003215. https://doi.org/10.1029/2022SW003215

Palmerio, E., Maharana, A., Lynch, B. J., Scolini, C., Good, S. W., Pomoell, J., et al. (2023). Modeling a Coronal Mass Ejection from an Extended Filament Channel. II. Interplanetary Propagation to 1 au. *The Astrophysical Journal*, *958*(1), 91. https://doi.org/10.3847/1538-4357/ad0229

Palmerio, E., Nieves-Chinchilla, T., Kilpua, E. K. J., Barnes, D., Zhukov, A. N., Jian, L. K., et al. (2021). Magnetic structure and propagation of two interacting CMEs from the Sun to Saturn. *Journal of Geophysical Research: Space Physics*, *126*(11), e2021JA029770. https://doi.org/10.1029/2021JA029770

Palmerio, E., Nitta, N. V., Mulligan, T., Mierla, M., O'Kane, J., Richardson, I. G., et al. (2021). Investigating remote-sensing techniques to reveal stealth coronal mass ejections. *Frontiers in Astronomy and Space Sciences*, *8*, 695966. https://doi.org/10.3389/fspas.2021.695966

Pesnell, W. D., Thompson, B. J., & Chamberlin, P. C. (2012). The solar dynamics observatory (SDO). *Solar Physics*, *275*(1–2), 3–15. https://doi.org/10.1007/s11207-011-9841-3

Potemra, T. A. (1994). Sources of large-scale birkeland currents. In J. A. Holtet & A. Egeland (Eds.), *Physical signatures of magnetospheric boundary layer processes* (pp. 3–27). Springer Netherlands. https://doi.org/10.1007/978-94-011-1052-5_1

Richardson, I. G., & Cane, H. V. (1995). Regions of abnormally low proton temperature in the solar wind (1965-1991) and their association with ejecta. *Journal of Geophysical Research*, *100*(A12), 23397–23412. https://doi.org/10.1029/95JA02684

Richmond, A. D. (2021). Joule heating in the thermosphere. In W. Wang (Ed.), *Upper atmosphere dynamics and energetics* (Vol. 4, p. 3). https://doi.org/10.1002/9781119815631.ch1

Riley, P., Baker, D., Liu, Y. D., Verronen, P., Singer, H., & Güdel, M. (2018). Extreme space weather events: From cradle to grave. *Space Science Reviews*, *214*(1), 21. https://doi.org/10.1007/s11214-017-0456-3

Roy, S., & Nandy, D. (2023). A time-efficient, data-driven modeling approach for predicting the geomagnetic impact of coronal mass ejections. *The Astrophysical Journal Letters*, *950*(2), L11. https://doi.org/10.3847/2041-8213/acd77c

Schrijver, C. J., Kauristie, K., Aylward, A. D., Denardini, C. M., Gibson, S. E., Glover, A., et al. (2015). Understanding space weather to shield society: A global road map for 2015-2025 commissioned by COSPAR and ILWS. *Advances in Space Research*, *55*(12), 2745–2807. https://doi.org/10.1016/j.asr.2015.03.023

Siemes, C., de Teixeira da Encarnação, J., Doornbos, E., Van Den Ijssel, J., Kraus, J., Pereštý, R., et al. (2016). Swarm accelerometer data processing from raw accelerations to thermospheric neutral densities. *Earth Planets and Space*, *68*, 1–16. https://doi.org/10.1186/s40623-016-0474-5

Smith, C. W., & Ness, N. F. (2022). Ace magnetic field (mag) geocentric solar ecliptic, gse, and geocentric solar magnetospheric, gsm, coordinates, level 2 (h1), 4 min data [Dataset]. NASA Space Physics Data Facility. https://doi.org/10.48322/brf1-g493

Stone, E. C., Frandsen, A. M., Mewaldt, R. A., Christian, E. R., Margolies, D., Ormes, J. F., & Snow, F. (1998). The advanced composition explorer. *Space Science Reviews*, *86*(1/4), 1–22. https://doi.org/10.1023/A:1005082526237

Sutton, E. K. (2009). Normalized force coefficients for satellites with elongated shapes. *Journal of Spacecraft and Rockets*, *46*(1), 112–116. https://doi.org/10.2514/1.40940

Thernisien, A. F. R., Howard, R. A., & Vourlidas, A. (2006). Modeling of flux rope coronal mass ejections. *The Astrophysical Journal*, *652*(1), 763–773. https://doi.org/10.1086/508254

Thompson, B. J., Cliver, E. W., Nitta, N., Delannée, C., & Delaboudinière, J. P. (2000). Coronal dimmings and energetic CMEs in April-May 1998. *Geophysical Research Letters*, *27*(10), 1431–1434. https://doi.org/10.1029/1999GL003668

Tóth, G., Sokolov, I. V., Gombosi, T. I., Chesney, D. R., Clauer, C. R., de Zeeuw, D. L., et al. (2005). Space weather modeling framework: A new tool for the space science community. *Journal of Geophysical Research*, *110*(A12), A12226. https://doi.org/10.1029/2005JA011126

Tóth, G., van der Holst, B., Sokolov, I. V., De Zeeuw, D. L., Gombosi, T. I., Fang, F., et al. (2012). Adaptive numerical algorithms in space weather modeling. *Journal of Computational Physics*, *231*(3), 870–903. https://doi.org/10.1016/j.jcp.2011.02.006

Tsurutani, B. T., Gonzalez, W. D., Gonzalez, A. L. C., Guarnieri, F. L., Gopalswamy, N., Grande, M., et al. (2006). Corotating solar wind streams and recurrent geomagnetic activity: A review. *Journal of Geophysical Research*, *111*(A7), A07S01. https://doi.org/10.1029/2005JA011273

Tsurutani, B. T., Green, J., & Hajra, R. (2022). The possible cause of the 40 SpaceX Starlink satellite losses in February 2022: Prompt penetrating electric fields and the dayside equatorial and midlatitude ionospheric convective uplift. arXiv e-prints, arXiv:2210.07902. https://doi.org/10.48550/arXiv.2210.07902

Tsyganenko, N. A., Andreeva, V. A., Sitnov, M. I., & Stephens, G. K. (2022). Magnetosphere distortions during the "satellite killer" storm of February 3-4, 2022, as derived from a hybrid empirical model and archived data mining. *Journal of Geophysical Research: Space Physics*, *127*(12), e2022JA031006. https://doi.org/10.1029/2022JA031006

Vandas, M., Romashets, E., & Geranios, A. (2015). Modeling of magnetic cloud expansion. *Astronomy and Astrophysics*, *583*, A78. https://doi.org/10.1051/0004-6361/201425594

Vasyliūnas, V. M., & Song, P. (2005). Meaning of ionospheric Joule heating. *Journal of Geophysical Research*, *110*(A2), A02301. https://doi.org/10.1029/2004JA010615

Wang, Y., Zhang, Q., Liu, J., Shen, C., Shen, F., Yang, Z., et al. (2016). On the propagation of a geoeffective coronal mass ejection during 15–17 March 2015. *Journal of Geophysical Research: Space Physics*, *121*(8), 7423–7434. https://doi.org/10.1002/2016JA022924

Wang, Y. M., Ye, P. Z., & Wang, S. (2003). Multiple magnetic clouds: Several examples during March–April 2001. *Journal of Geophysical Research*, *108*(A10), 1370. https://doi.org/10.1029/2003JA009850

Zesta, E., & Oliveira, D. M. (2019). Thermospheric heating and cooling times during geomagnetic storms, including extreme events. *Geophysical Research Letters*, *46*(22), 12739–12746. https://doi.org/10.1029/2019GL085120

Zhang, J., Richardson, I. G., Webb, D. F., Gopalswamy, N., Huttunen, E., Kasper, J. C., et al. (2007). Solar and interplanetary sources of major geomagnetic storms (Dst < = -100 nT) during 1996-2005. *Journal of Geophysical Research*, *112*(A10), A10102. https://doi.org/10.1029/2007JA012321

Zhang, Y., Paxton, L. J., Schaefer, R., & Swartz, W. H. (2022). Thermospheric conditions associated with the loss of 40 Starlink satellites. *Space Weather*, *20*(10), e2022SW003168. https://doi.org/10.1029/2022SW003168